Fabrication of three-dimensional ordered nanodot array structures by a thermal dewetting method

Fabrication of three-dimensional ordered nanodot array structures by a thermal dewetting method

Zhenxing Li, Masahiko Yoshino and Akinori Yamanaka

Department of Mechanical and Control Engineering, Tokyo Institute of Technology, 2-12-1 Ookayama, Meguro-ku, Tokyo 152-8552, Japan

E-mail: li.z.ae@m.titech.ac.jp, myoshino@mes.titech.ac.jp and ayamanaka@mes.titech.ac.jp

Abstract
A new fabrication method for three-dimensional nanodot arrays with low cost and high throughput is developed in this paper. In this process, firstly a 2D nanodot array is fabricated by combination of top-down and bottom-up approaches. A nanoplastic forming technique is utilized as the top-down approach to fabricate a groove grid pattern on an Au layer deposited on a substrate, and self-organization by thermal dewetting is employed as the bottom-up approach. On the first-layer nanodot array, SiO_2 is deposited as a spacer layer. Au is then deposited on the spacer layer and thermal dewetting is conducted to fabricate a second-layer nanodot array. The effective parameters influencing dot formation on the second layer, including Au layer thickness and SiO_2 layer thickness, are studied. It is demonstrated that a 3D nanodot array of good vertical alignment is obtained by repeating the SiO_2 deposition, Au deposition and thermal dewetting. The mechanism of the dot agglomeration process is studied based on geometrical models. The effects of the spacer layer thickness and Au layer thickness on the morphology and alignment of the second-layer dots are discussed.

(Some figures may appear in colour only in the online journal)

1. Introduction

Nanodot arrays are attracting attention because of their potential in optical, electrical and magnetic devices. Many studies have shown the possibility of using nanodot arrays to address current environmental and social problems. For instance, solar cell efficiency can be improved by using a nanodot array because the bandgap of the solar cell can be tuned by the morphology of the nanodots so as to collect more photon energy [1, 2]. A nanodot array of magnetic material can be utilized as a high-density patterned media. It can achieve very high data storage [3, 4]. Another important example is nanodot arrays of noble metals. It is known that they exhibit unique optical properties, such as localized surface plasmon resonance (LSPR) [5, 6], surface-enhanced Raman spectroscopy (SERS) [7–9] and surface-enhanced fluorescence (SEF) [10, 11]. These phenomena are applied to many plasmonic devices, such

as solar cells [12, 13], plasmonic LEDs [14, 15] and plasmonic biosensors [16]. In addition, it is expected that these performances can be improved drastically if these dots are aligned in three-dimensional structures [17–19]. Based on these expectations, efficient fabrication technologies for three-dimensional (3D) nanodot arrays are eagerly desired.

Nanodot arrays can be fabricated by various methods. Two strategies for nanofabrication can be identified, namely the top-down approach and the bottom-up approach. Top-down approaches, such as ultraviolet lithography, electron beam lithography (EBL) [20], and focused ion beam (FIB) [21, 22] are widely utilized in many nanofabrication processes. However, these processes are not always suitable for the fabrication of nanodot arrays because they need stringent control of process conditions, hazardous chemicals, and costly facilities. Another good example is nanoimprint lithography (NIL) [23, 24], which enables us fast and economical nanofabrication. However, the nanostructure mold
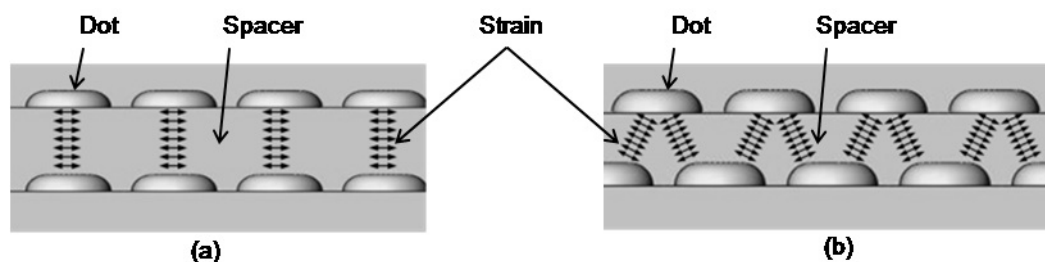
Figure 1. Schematic drawing of interlayer correlations of dots stacked in a multilayer structure. (a) Vertically aligned and (b) staggered stacking.

necessary in the NIL process is usually made by conventional lithography technologies. Hence NIL cannot overcome the disadvantages of conventional lithography processes. On the other hand, bottom-up approaches by self-organization processes are expected to be high-throughput, low-cost, less stringent technologies. For example, Stranski–Krastanov (SK) growth in the epitaxial growth of a semiconductor substrate, anodized aluminum oxide [25], colloidal lithography [26], thermal dewetting and other chemical processes are extensively studied. However, these self-organization methods have serious disadvantages, such as poor regularity and low uniformity of dots. In order to overcome these disadvantages, some researchers have developed new processes combining the top-down approach with the bottom-up approach. Lin *et al* proposed a combination of FIB machining and thermal dewetting [27]. Zhong *et al* reported a combination of lithography and self-assembly techniques that realized regulated Ge islands on prepatterned silicon substrates [28, 29]. Giermann and Thompson developed well-ordered nanodot arrays made by solid-state dewetting on patterned templates [30, 31]. However, they utilized FIB or other lithography methods in their top-down processes, and disadvantages still remained in their combination processes. Some of the present authors developed a top-down/bottom-up combination process for fabrication of a 2D ordered nanodot array, in which they employed nanoplastic forming (NPF) as the top-down process and thermal dewetting as the bottom-up process [32, 33]. Since NPF is a kind of precision metal-forming technique, it is expected that this method will achieve a rapid and low-emission process with the advantage of low cost and high throughput.

Although many researchers have developed new nanofabrication technologies, only a few researchers have attempted the fabrication of 3D nanodot arrays. Bottom-up methods such as wet coating processes [34–36] have been extensively studied to synthesis multilayer nanoparticle films. But the regularity and uniformity of the nanoparticle arrays were not sufficient. Epitaxial growth is another important self-organization method to fabricate multilayer nanodot arrays. Under certain conditions, dots are aligned in vertical or staggered positions, as shown in figure 1 [37]. If a similar vertical alignment mechanism works also on the thermal dewetting process, a 3D metallic nanodot array can be fabricated by a low-cost, high-throughput method.

The objective of this paper is to develop a new fabrication process for 3D metallic nanodot arrays by a thermal dewetting method, and to study the dot formation mechanism in vertical alignment. In this paper, a new thermal dewetting process is studied for the fabrication of 3D nanodot arrays. An experiment is conducted using gold as the dot material and SiO_2 as the material of the spacer layers. By repeating the thermal dewetting of the Au layer and SiO_2 coating as a spacer layer, multilayer nanodot array formation is examined. The effects of process conditions on nanodot formation in the upper layer are studied. By optimizing the effective parameters on vertical alignment of the nanodot array, fabrication of a 3D nanodot array with four layers is successfully demonstrated. Based on the experimental results, the mechanisms of vertical alignment of the second-layer dots are discussed.

2. Experimental processes

2.1. The proposed procedure

Figure 2 shows the fabrication process of a multilayer nanodot array examined in this paper. Firstly, a 2D nanodot array is fabricated on a quartz glass substrate by the top-down/bottom-up combination process. As shown in figure 2(a), this process comprises three steps: (1) deposition of a metal film on a substrate by sputter coating, (2) patterning of a square nano-groove grid on the deposited metal film by the nanoplastic forming (NPF) technique, (3) annealing of the patterned substrate in an electric furnace to cause dot aggregation. Through this procedure, the deposited metal film is agglomerated to a nanodot array by a self-organization mechanism. The dot size and dot alignment can be controlled by adjusting the NPF conditions.

Secondly, the second layer and upper layer are fabricated by the process shown in figure 2(b): (4) deposition of a SiO_2 spacer layer on the first-layer nanodot array by sputter coating, (5) deposition of a metal film layer on the SiO_2 spacer layer by a sputter coater, (6) annealing of the specimen to cause dot agglomeration on the spacer layer. (7) Multilayer is fabricated by repeating the above-mentioned steps from (4) SiO_2 deposition to (6) annealing. It is noted that the nanodot array is formed on the spacer layer without NPF grid patterning.

2.2. Experimental conditions

In this experiment, gold (Au) was used as the dot material, and quartz glass was used as the substrate material. The substrate
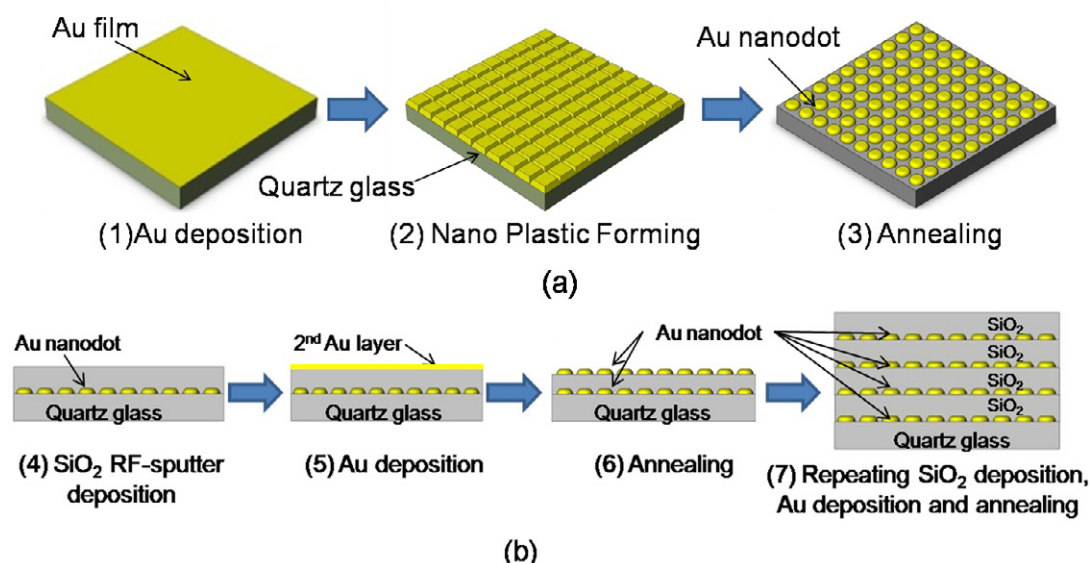
Figure 2. Schematic diagram of 3D nanodot array fabrication process. (a) First-layer nanodot array formation, (b) multilayer nanodot array formation.

was made from a quartz slide glass, and cut to a size of 12 mm × 12 mm × 1 mm. The thickness is 1 mm. Its surface was finished to optical flatness by the maker (Matsunami Glass Ind., Ltd). The substrate was ultrasonically cleaned in an acetone bath before it was applied to the experiment. In steps (1) and (5), Au was deposited on the substrate by using a DC sputter coater. The sputter gas was argon (Ar) and the pressure was 15 Pa. The distance between the specimen and the Au target was 35 mm. In the experiment, the thickness of the Au film was controlled from 10 to 25 nm by adjusting the sputtering time. For the measurement of the film thickness, before the experiments, Au is deposited by DC sputter on a substrate on which some parts of the film are peeled off. The profile of the step between the coated and peeled-off surface is measured by atomic force microscopy (AFM, Keyence VN-8000). The deposition rate is calculated based on the AFM data.

Figure 3 shows the NPF equipment used for the grid patterning on a deposited metal film. Details of the equipment are explained in [32, 33]. A single-crystal diamond knife-edge tool shown in figure 3 was used for the experiment. Its width is 1.5 mm, and its edge angle is 60°. Its edge is ground very sharp, and the edge radius is around 50 nm. Firstly, a series of parallel nano-grooves was fabricated on the metal film by indenting with the diamond tool. The indentation load was controlled at 1 N so that the tool was indented only to the metal film layer and it did not damage the quartz glass substrate. Then, the substrate was rotated laterally through 90°, and another series of parallel grooves was indented again on the prepatterned grooves. The distance between the grooves was 200 nm in this experiment, and a square groove grid was fabricated on the metal film.

Thermal dewetting was conducted by annealing in an electric furnace under ambient atmosphere. Two annealing temperatures were examined in the experiment, 700 and 800 °C. The annealing time was 10 min. A SiO$_2$ spacer
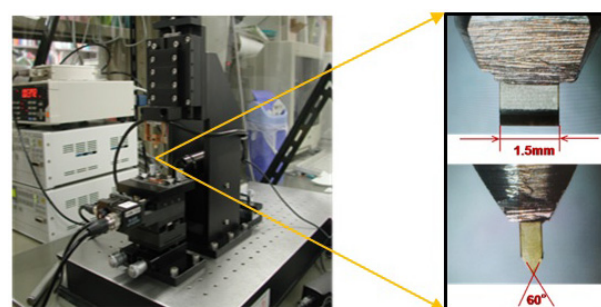

Figure 3. Picture of nanoplastic forming equipment and the diamond knife-edge tool.

Table 1. Experimental conditions of the first-layer nanodot array formation.

Thickness of gold layer (nm)	Grid size (nm)	Indentation load (N)	Annealing temperature (°C)	Annealing time (min)
10	200	1	700, 800	10

layer was deposited on the first-layer nanodot array using a RF-sputter coater. The sputtering gas was Ar. The gas pressure was 10 Pa. In order to investigate the influence of the thickness of the spacer layer on dot formation in the second layer, the thickness is controlled from 25 to 300 nm by adjusting the coating time. Table 1 summarizes the experimental conditions of the first-layer nanodot array formation, and table 2 gives those of the second-layer nanodot array formation.

The morphology of the dot array was characterized using a field-emission scanning electron microscope (FE-SEM, JSM-6301F JEOL). As for observation of the cross section, the specimen was machined by focused ion beam (FIB) etching normal to the surface of the specimen, and then the
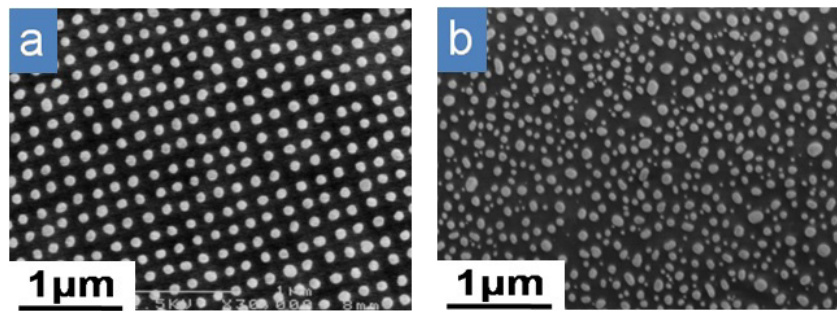
Figure 4. FE-SEM image of ordered nanodot array (a) annealed with NPF, and random dots (b) without NPF.
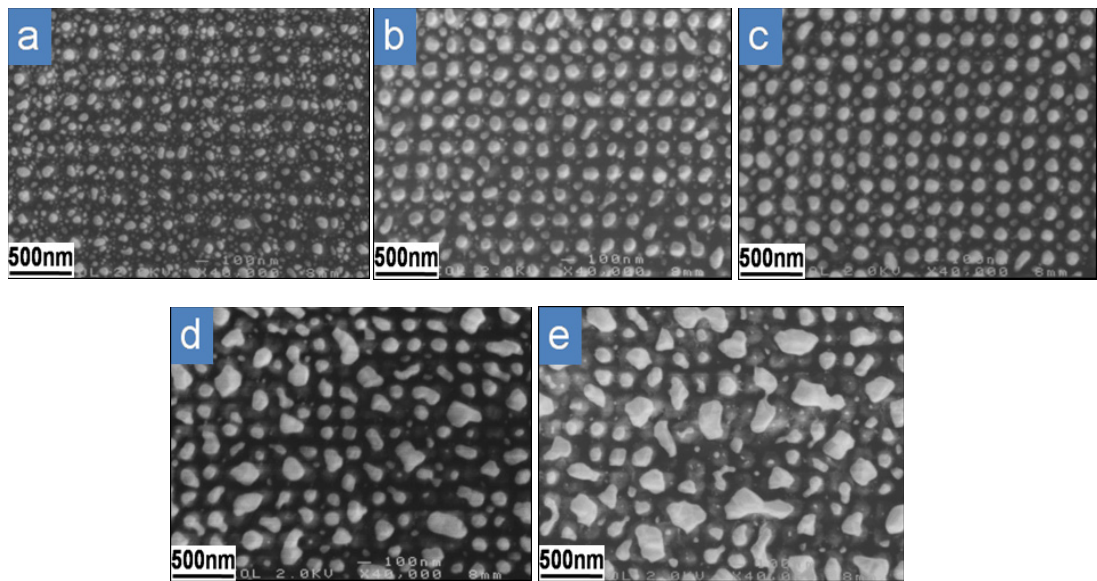

Figure 5. FE-SEM micrographs of morphology of second-layer dots with various Au layer thicknesses: (a) 10 nm, (b) 15 nm, (c) 17 nm, (d) 20 nm and (e) 25 nm. The thickness of the SiO$_2$ spacer layer is 100 nm for all specimens. Annealing at 700 °C for 10 min.

Table 2. Experimental conditions of the second-layer nanodot array formation.

Thickness of SiO$_2$ spacer layer (nm)	Thickness of gold layer (nm)	Annealing temperature (°C)	Annealing time (min)
25, 50, 100, 150, 200, 300	10, 12, 15, 17, 20, 25	700, 800	10

sample stage was tilted by around 50° and the cross section was observed by the FE-SEM.

3. Experimental results

3.1. Morphology of the first layer dots

Figure 4(a) shows FE-SEM images of an ordered nanodot array fabricated by NPF patterning and subsequent thermal dewetting at 800 °C for 10 min. It is found that the size of dots is uniform. The mean diameter is about 100 nm and the relative standard deviation of dot size is around 0.05. They are aligned at the center of the grid pattern on

the substrate. The center-to-center interparticle distance is 200 nm, which is consistent with the grid size. On the other hand, figure 4(b) shows the nanodots formed without grid patterning for comparison. The uniformity of dot size and regularity of dot alignment are poor in figure 4(b). It is apparent that grid patterning is efficient in improving the regularity of the nanodot array. The specimens with the ordered nanodot array, as shown in figure 4(a), were used for the following experiments to fabricate double-layer and multilayer dot array structures.

3.2. Influence of Au layer thickness on second layer dots formation

Figure 5 shows SEM images of Au nanodot arrays formed on the SiO$_2$ spacer layer. The thickness of Au layer was (a) 10 nm, (b) 15 nm, (c) 17 nm, (d) 20 nm and (e) 25 nm. The thickness of the spacer layer was 100 nm for all specimens. The annealing temperature was 700 °C. The annealing time was 10 min. In figure 5(a), the gold layer was agglomerated into random multiple dots and the regularity of the dot alignment was poor. In figure 5(b), when thickness of the Au layer is 15 nm, larger dots with improved regularity
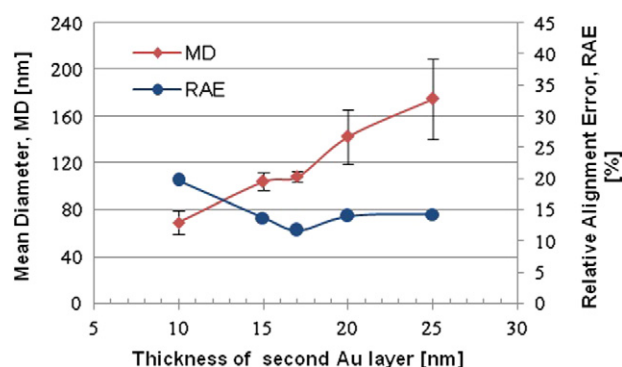
Figure 6. Variation of the average diameter and RAE of second-layer nanodots against the thickness of second Au layer. The thickness of the SiO$_2$ spacer layer is 100 nm. Annealing at 700 °C for 10 min.

are observed. However, the distortion of the dots is fairly large, and smaller dots are found between the larger dots. In figure 5(c), when the thickness is 17 nm, regularity and uniformity is improved and dots are aligned on a grid pattern. As shown in figures 5(d) and (e), when the thickness of Au layer is further increased, some dots are connected with adjacent dots and their regularity becomes poor.

Figure 6 shows the variation of MD (mean diameter) and RAE (relative alignment error) of second-layer nanodots against the thickness of Au layer. The MD is analyzed from the SEM images. The vertical bar on each plot indicates the standard deviation of the dot diameters. RAE is the mean square of the deviation from the ideal position, i.e. the square grid pattern. The RAE represents the degree of regularity quantitatively [33]. It is confirmed that the mean diameter increases with the increase of Au layer thickness. The standard deviation decreases with the increase of Au thickness when the thickness is smaller than 17 nm. The standard deviation increases when the Au layer becomes thicker than 20 nm. As for the RAE, it becomes minimized when the thickness is 17 nm.

Figue 7 shows the cross sections of double-layer dots with various second-layer Au thicknesses. The white region is Au, while the dark region is SiO$_2$. In figure 7(a), the second-layer Au thickness is 10 nm. Small nanodots are dispersed randomly above the first-layer nanodot array. It is found from the figure that the morphology of the spacer layer is composed of mounds and troughs in accordance with the dot position on the first layer. In addition, the cross section of nanodots on the first layer is oval, and the top of the dot is fairly flat. Small dots are formed on the surface of the spacer layer anywhere on the mounds and troughs. Figure 7(b) shows the cross section of the dot array of figure 5(c), when the second-layer Au thickness is 17 nm. It is apparent that the second-layer dots are located above the first-layer dots. This indicates that dots are formed on the mounds of the spacer layer. In figure 7(c), when the second-layer Au thickness is 25 nm, some dots on the spacer layer merged with adjacent dots, and form larger dots.

3.3. Influence of SiO$_2$ spacer layer thickness on second layer dots formation

Figure 8 shows the FE-SEM images of second-layer Au dots on the SiO$_2$ layers of various thicknesses. The thickness of Au layer was 12 nm for all specimens. The annealing temperature was 800 °C and the annealing time was 10 min. In figure 8(a), when the thickness of the spacer layer is 25 nm, the regularity of dot alignment and uniformity of dots is poor. In figure 8(b), when the thickness of the spacer layer is 50 nm, the regularity of the dots is improved. In figure 8(c), when the SiO$_2$ spacer layer thickness is 100 nm, the larger dots are aligned on the grid pattern. Small dots are also formed between larger dots. It is considered that the large dots are formed on the mounds and that the small dots are formed in the troughs. Figure 8(d) shows that dots are aligned exactly on the grid pattern when the spacer layer thickness is 150 nm. The dots in the troughs become much smaller and almost vanish. In figure 8(e), when the spacer layer is 300 nm, some dots are
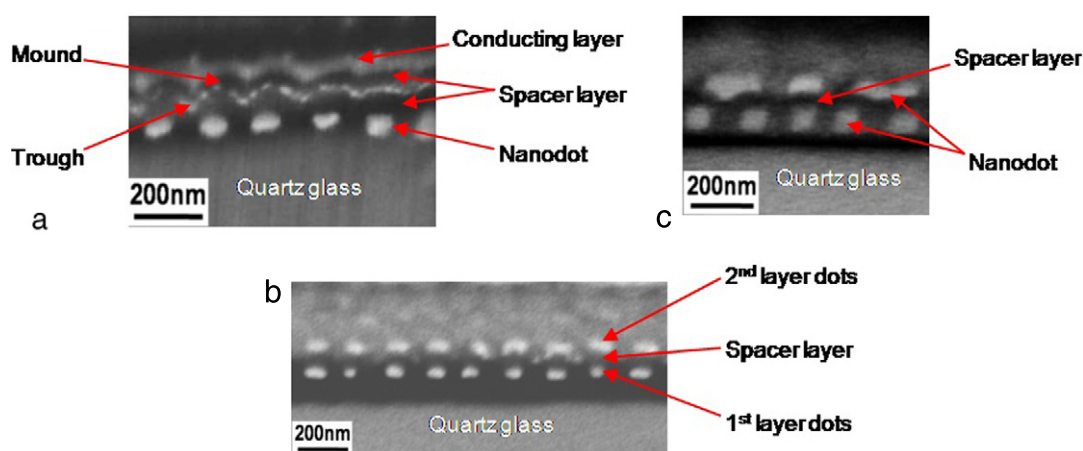

Figure 7. FE-SEM micrographs of cross-sections of double-layer nanodots. The second-layer Au thickness is (a) 10 nm, (b) 17 nm and (c) 25 nm.
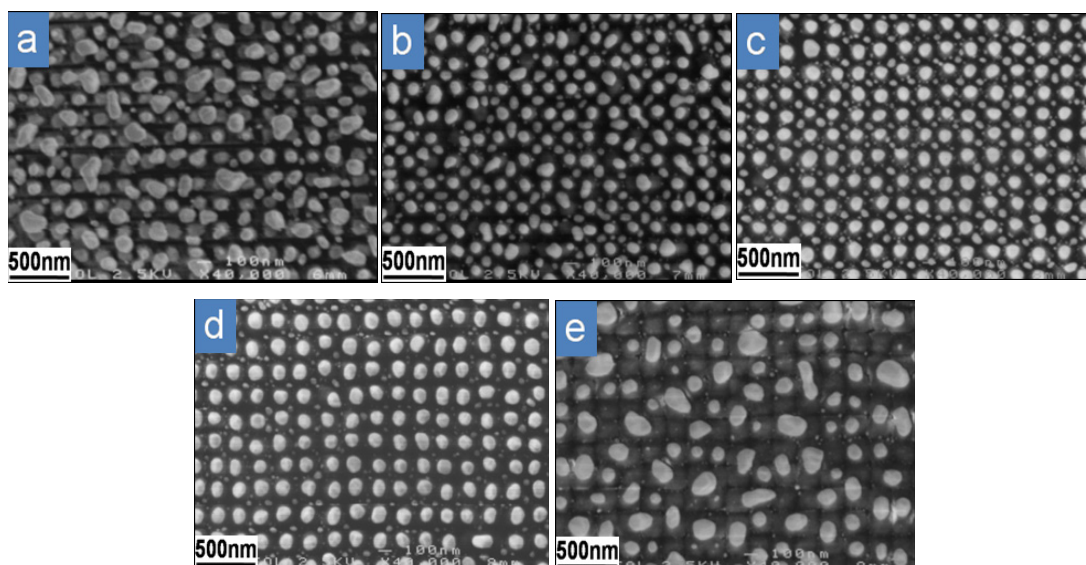
Figure 8. FE-SEM micrographs of morphology of second-layer dots with various SiO_2 spacer layer thicknesses. The thickness of the SiO_2 spacer layer is (a) 25 nm, (b) 50 nm, (c) 100 nm, (d) 150 nm and (e) 300 nm. The thickness of the Au layer is 12 nm for all specimens. Annealing at 800 °C for 10 min.

merged with adjacent dots, and the regularity of the array deteriorates.

Figure 9 summarizes the variation of the mean diameter and RAE of second-layer nanodots against the thickness of the spacer layer. It is confirmed that the standard deviation becomes smaller when the thickness of the spacer layer increases from 30 to 100 nm. The standard deviation is minimized when the thickness of the spacer layer is 100 nm, and the standard deviation increases when the spacer layer becomes thicker than 150 nm. In addition, the RAE decreases with the increase of spacer layer thickness when the thickness is smaller than 100 nm. The RAE is minimized when the thickness of the spacer layer is 150 nm. The RAE increases with the increase of spacer thickness when the layer is thicker than 150 nm. Good regularity is obtained when the thickness is between 50 and 200 nm.

3.4. Multilayer dot fabrication

The feasibility of the thermal dewetting method for fabrication of a multilayer nanodot array was examined. As for the first layer, an ordered nanodot array was fabricated by NPF and subsequent thermal dewetting at 800 °C for 10 min. Then, a SiO_2 spacer layer was coated on the first-layer nanodot array to a thickness of 100 nm. Au was then coated on the spacer layer to a thickness of 12 nm, and annealed at 800 °C for 10 min. By repeating SiO_2 deposition, Au deposition and thermal dewetting three times, a four-layer nanodot array was fabricated. Figure 10(a) shows the FE-SEM micrograph of the nanodot array on the fourth layer. Good lateral regularity and uniformity of dot size are confirmed. It is shown that there are very small dots (residue) formed between the ordered nanodot arrays at the same layer. This Au residue will influence the subsequent dot formation on the layers and may affect the performance of the nanodot
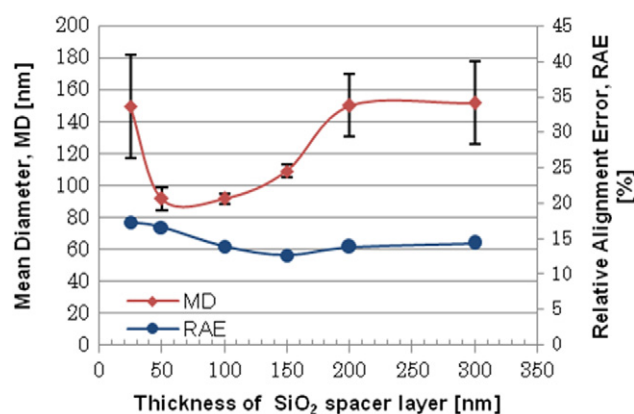

Figure 9. Variation of the average diameter and RAE of second-layer nanodots against the thickness of spacer layer. The thickness of the Au layer is 12 nm. Annealing at 800 °C for 10 min.

array for future practical applications. The residue can be reduced by controlling process conditions such as the spacer layer thickness and Au layer thickness adequately. Also, some etching techniques could be effective in eliminating the residue. Au atoms can diffuse into SiO_2 by thermal annealing from the statistical point of view. It is difficult to confirm the existence of Au atoms in the substrate in our experiment, but it is considered that they are so few that they will not affect the performance of the nanodot array. According to some previous literature on the dewetting process of Au on silica [38, 39], the Au diffusion into SiO_2 during annealing is very weak and negligible. Figure 10(b) shows a cross section of the four-layer nanodot array. The white region is Au, while the dark region is SiO_2. The topmost layer is a Au layer deposited to maintain conductivity for the FIB machining. It is confirmed that the nanodots are aligned regularly in the vertical direction in four layers. A 3D nanodot array with good
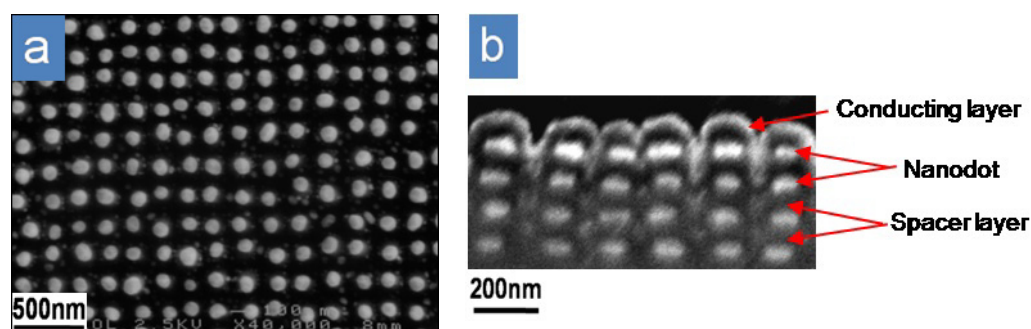
Figure 10. FE-SEM micrographs of morphology of fourth-layer dots (a) and cross section of four-layer dots (b).
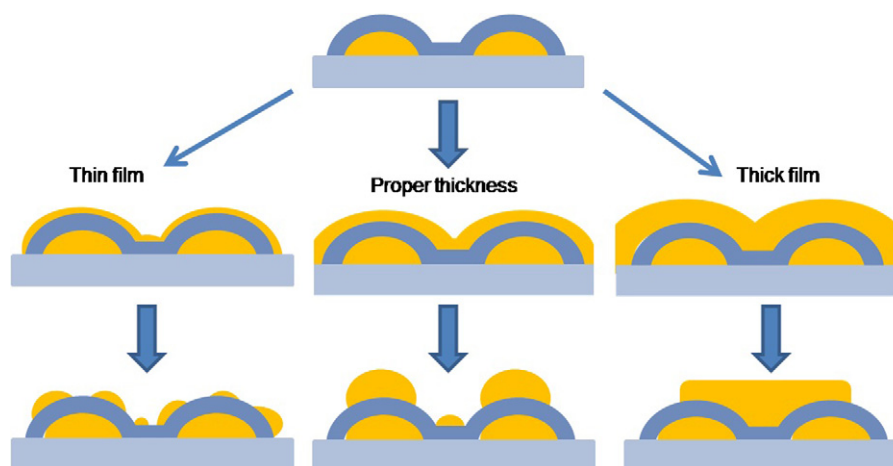

Figure 11. Schematic illustration of second-layer dot formation for different Au layer thickness.

lateral and vertical alignment was successfully fabricated by this method. By controlling the experimental conditions adequately, more multiple layers of ordered nanodot array can be fabricated by this method. However, in practice, since the dot formation on the upper layers is affected by the morphology of the dots on the lower layers, the dot alignment will be degraded gradually due to distortion or misalignment of dots in the repeated processes.

4. Discussion of dot formation

4.1. Effect of second layer Au thickness on dot formation

From the experimental results, it was found that the morphology of the second-layer nanodots is affected by the thickness of the second Au layer and the thickness of the spacer layer. Figure 11 illustrates three types of dot formation patterns attributed to difference of the deposited Au film thickness. In the case that the deposited Au film is very thin, the film is separated into many small dots. It is known that many small holes exist in a deposited Au film when its thickness is very small [30, 31]. Separation of a metal film is initiated from these holes, and each part of the separated Au film is agglomerated into a nanodot. Therefore the average nanodot size depends on the initial film thickness [40, 41]. When the deposited Au film thickness is very thin, the dot size is much smaller than the size of the mound. As a result, dots

are formed randomly on the mounds, as seen in figure 5(a). In case that the Au film is of ideal thickness, the dot size is almost equal to the size of the mounds. The dots are formed on the top of the mound, and they are aligned in the same grid pattern as the dot array on the first layer, as seen in figure 5(c). It is considered that the Au film thickness is thin at the circumference of the mounds because the surface of the mound top is flat but the surface of the circumference of the mounds is inclined. Since the thin part of a film is easily separated in the dewetting process, the metal film on a mound is separated along the circumference, and agglomerated into a dot. The outside part of the mound is agglomerated into dots in the trough, as seen in figure 5(c). In the case that the film is too thick, the dot size becomes larger than the size of the mound, and the dots are connected to the adjacent dots. These dots merge and form a large dot, and as a result their alignment becomes random, as seen in figure 5(e).

4.2. Effect of spacer layer thickness on dot formation

Figure 12 illustrates three types of dot formation patterns attributed to differences of the spacer layer thickness. When the spacer layer is quite thin, the troughs among the mounds are connected each other. Atoms of the metal film can move along the troughs and become agglomerated at arbitrary positions on the spacer layer. Comparatively large dots are formed in the troughs, and located randomly, as seen in
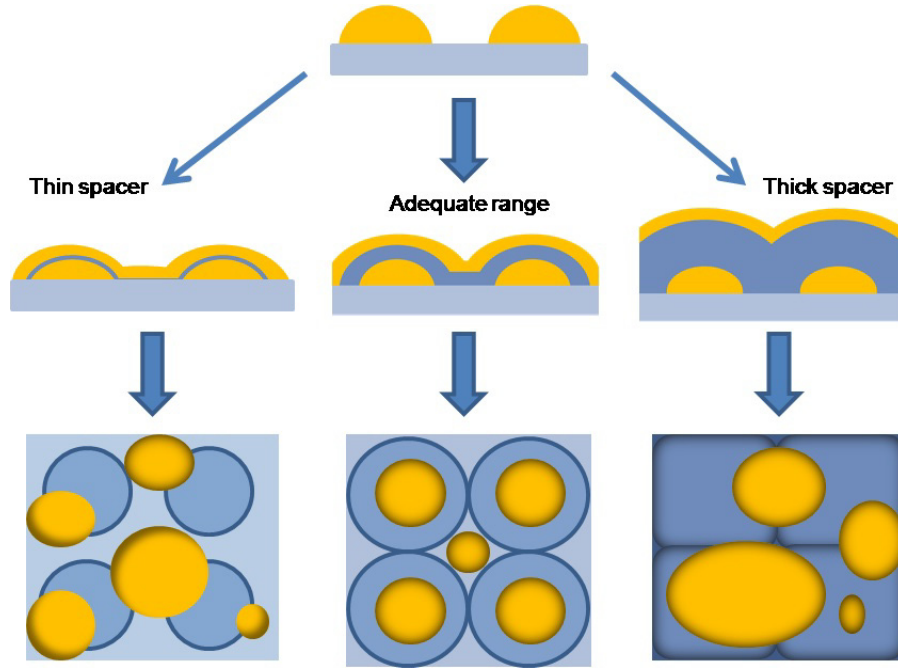
Figure 12. Schematic illustration of second-layer dot formation on spacer layers of various thicknesses.

figure 8(a). When the thickness of the spacer layer is in the ideal range, the troughs are isolated from the adjacent troughs by the mounds, and a small dot is formed in the trough. The metal film on a mound forms a large dot, as seen in figure 8(c). When the spacer layer is very thick, the surface of the spacer layer becomes almost flat, and the regularity of the first layer dots does not affect the alignment of dots on the spacer layer. As a result, dots are formed randomly on the spacer layer, the same as on the flat substrate, as seen in figure 8(e).

Figure 13 shows dots agglomerated on the spacer layer of ideal thickness. In this model, the distance of the centers of dots is P, the diameter of the first-layer nanodot array is D, the thickness of the SiO$_2$ spacer layer is t_s, and thickness of the second Au layer is t_{au}. The black square shown in figure 13(a) is a basic unit of the model. It is assumed that the Au film in the orange dashed square (side length is L) is agglomerated into a dot in the trough and the remaining parts of the film in the unit area are agglomerated into dots on the mounds. Based on assumption that volume of the Au film is conserved throughout the dewetting process, the volume of the Au film in the orange square is equal to the volume of the smaller dot (diameter is D_s) aggregated in a trough. In the meantime, the volume of the remaining parts of the film in the unit area is equal to the volume of the larger dot (diameter is D_l) on a mound. These relationships are expressed by the following equations.

$$L^2 t_{au} = \frac{\pi D_s^3}{24 \sin^3 \theta}(2 - 3\cos\theta + \cos^3\theta)$$
$$(0° < \theta \leq 90°) \tag{1}$$

$$(P^2 - L^2)t_{au} = \frac{\pi D_l^3}{24 \sin^3 \theta}(2 - 3\cos\theta + \cos^3\theta)$$
$$(0° < \theta \leq 90°). \tag{2}$$

The diameter of a dot in a trough D_s and the diameter of a dot on a mound D_l are calculated as follows,

$$D_s = \left(\frac{24L^2 t_{au}\sin^3\theta}{\pi(2 - 3\cos\theta + \cos^3\theta)} \right)^{\frac{1}{3}} \quad (0° < \theta \leq 90°) \tag{3}$$

$$D_l = \left(\frac{24(P^2 - L^2)t_{au}\sin^3\theta}{\pi(2 - 3\cos\theta + \cos^3\theta)} \right)^{\frac{1}{3}} \quad (0° < \theta \leq 90°) \tag{4}$$

where θ is the contact angle of Au dots on the SiO$_2$ spacer layer.

Figure 14 compares the calculated dot diameter with the experimental data. The following parameters are used for this calculation; $P = 200$ nm, $D = 100$ nm, $t_{au} = 12$ nm and $\theta = 90°$. The solid curves show the variation of the calculated dot diameter against the spacer layer thickness. The symbols show the experimental data. It is found that the diameter of dots in the trough decreases with the increase of the spacer layer thickness. On the other hand, the diameter of dots on the mound increases with the increase of spacer thickness. These trends of diameter variation agree with the experimental data. It can be concluded that the morphology and alignment of second-layer dots is attributed to the topography of the spacer layer. Since the thickness of the spacer layer affects the topography of the spacer layer, the alignment and size of second-layer dots can be controlled by adjusting the spacer layer thickness.

4.3. Mechanism of dots aggregation on the mounds

As shown by the cross section in figure 10(b), the metal film on the spacer layer tends to be agglomerated on the top of
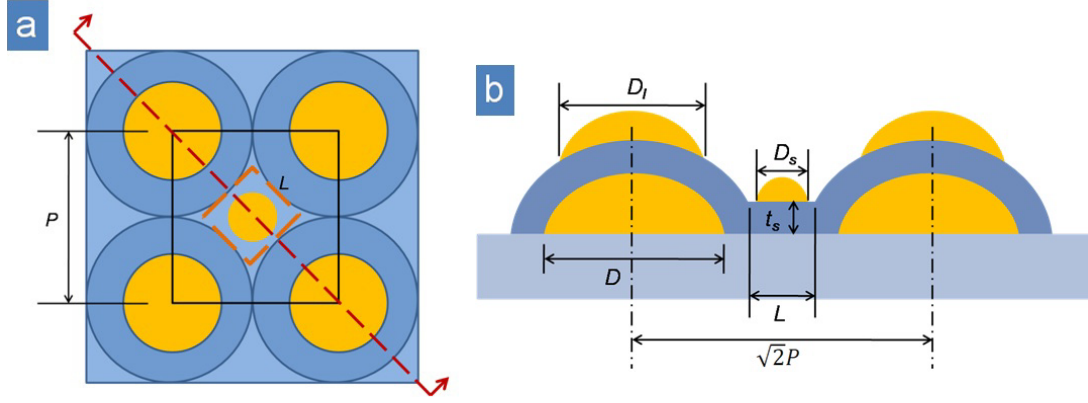
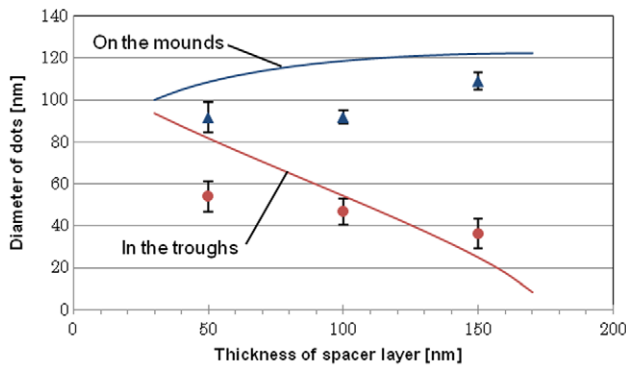**Figure 13.** Schematic drawing of top view (a) and cross section (b) for second-layer dot formation.

Figure 14. Variation of the diameter of second-layer nanodots in the troughs and on the mounds against the thickness of the spacer layer. The solid curves show the calculated results. The symbols show the experimental data.

the mound. Similar vertical alignment was reported in [37], in which the epitaxial growth method was utilized. They attributed the good vertical alignment to the stress distribution in the spacer layer, where stress is induced by the lattice mismatch between the dot material and the spacer material. However, the experiment presented in this paper employed the sputtering method for deposition of the spacer layer. Thus, the crystalline structure of the spacer layer is considered to be amorphous, and stress due to lattice mismatch cannot be the reason for the vertical alignment.

Another possibility is the difference of chemical composition between the deposited SiO_2 layer and the quartz glass substrate. The difference of chemical composition causes a difference of surface energy between the mound and the trough. The difference of surface energy can induce a metal film to be agglomerated on the mound. However, it is difficult to confirm a difference of chemical composition between the mound and the trough at the present stage. We would like to leave this matter outside of the scope of this paper.

Another possibility is surface curvature of the spacer layer. As seen in figure 10(b), the top of the mound is convex but the top of the mound is almost flat because the dot on the first layer is oval. The effect of surface curvature on dot

formation can be evaluated by the total free energy of the dot and substrate system. Figure 15 illustrates geometrical models of dots on (a) a convex substrate and (b) a concave substrate. They are axisymmetric models, and the surface of the substrate is spherical with radius R_0. t is the thickness of a metal layer. D_0 and D are the diameters of the metal film and a dot observed from the top view. It is assumed that the dot keeps a hemispherical shape during the agglomeration process. The radius of the dot is denoted by R. Angles ϕ, ϕ_0, ζ are defined as shown in the figure. θ_c is the contact angle between the dot and the substrate in the steady state. It is known that θ_c satisfies Young's equation.

$$\gamma_I - \gamma_S = -\gamma_M \cos\theta_c \tag{5}$$

where γ_M is the surface energy of the metal (dot), γ_S is the surface energy of the substrate, and γ_I is the interfacial energy between the metal (dot) and substrate.

In the case of the convex substrate model, the following equations are obtained from the geometrical relationship.

$$R \sin\zeta = R_0 \sin\phi \tag{6}$$
$$\theta_c = \phi - \zeta. \tag{7}$$

In the case of the concave substrate model, the following equation is obtained instead of (7),

$$\theta_c = \zeta + \phi. \tag{8}$$

The total free energy G of the system in the agglomeration process is expressed as the summation of the surface energy of a dot, the interfacial energy and surface energy of the exposed substrate. Hence,

$$G = S_M \gamma_M + S_I \gamma_I + (A - S_I)\gamma_S \tag{9}$$

where A is the area of the curved substrate, S_M is the area of metal (dot) surface, and S_I is the area of the dot–substrate interface. They are calculated by the following equations.

$$A = 2\pi R_0^2 (1 - \cos\phi_0) \tag{10}$$
$$S_M = 2\pi R^2 (1 - \cos\zeta) \tag{11}$$
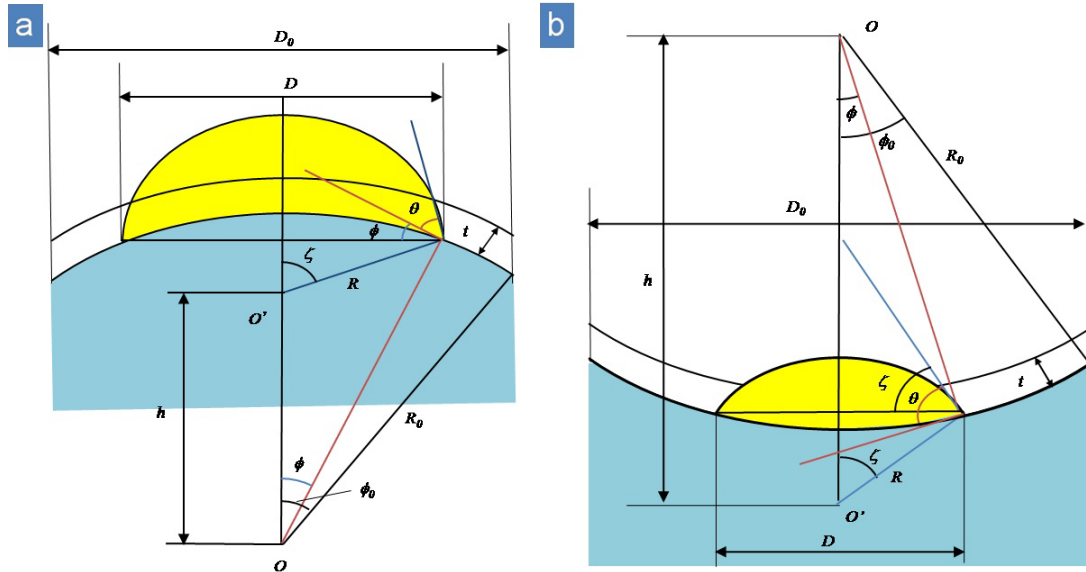$$S_I = 2\pi R_0^2 (1 - \cos\phi). \tag{12}$$

Figure 15. Geometrical models of nanodots on curved substrates. (a) A convex substrate and (b) a concave substrate.

By substituting (6), (10), (11) and (12) into (9), we obtain

$$G = 2\pi \left(\frac{R_0 \sin\phi}{\sin\zeta} \right)^2 (1 - \cos\zeta)\, \gamma_M - 2\pi R_0^2 (1 - \cos\phi)$$
$$\times \gamma_M \cos\theta_c + 2\pi R_0^2 (1 - \cos\phi_0)\gamma_S. \quad (13)$$

Here we assume that the volume of the metal layer is conserved throughout the agglomeration process. The following equation is obtained for the convex model

$$\frac{\pi}{3} \frac{R_0^3 \sin^3\phi}{\sin^3(\theta_c + \phi)} (2 - 3\cos(\theta_c + \phi) + \cos^3(\theta_c + \phi))$$
$$- \frac{\pi}{3} R_0^3 (2 - 3\cos\phi + \cos^3\phi) = 2\pi R_0^2 (1 - \cos\phi_0)t. \quad (14)$$

Similarly, the volume conservation of a dot on the concave substrate is

$$\frac{\pi}{3} \frac{R_0^3 \sin^3\phi}{\sin^3(\theta_c - \phi)} (2 - 3\cos(\theta_c - \phi) + \cos^3(\theta_c - \phi))$$
$$+ \frac{\pi}{3} R_0^3 (2 - 3\cos\phi + \cos^3\phi) = 2\pi R_0^2 (1 - \cos\phi_0)t. \quad (15)$$

Variation of the total free energy G was calculated by solving (14) and (15) against ϕ using Excel. In this calculation, the following values are used:

$$\gamma_M = 1 \times 10^{-18}\ \text{J nm}^{-2}, \qquad \gamma_s = 1 \times 10^{-18}\ \text{J nm}^{-2},$$
$$t = 10\ \text{nm}, \qquad D_0 = 100\ \text{nm},$$
$$\theta_c = 150°, 90°, 10°.$$

Figure 16 shows variation of the total free energy G against the radius of substrate R_0. It is found that G decreases rapidly with the increase of R_0, but becomes almost constant when R_0 is larger than 200 nm. This indicates that total free energy of the system decreases more on a flat substrate than on a
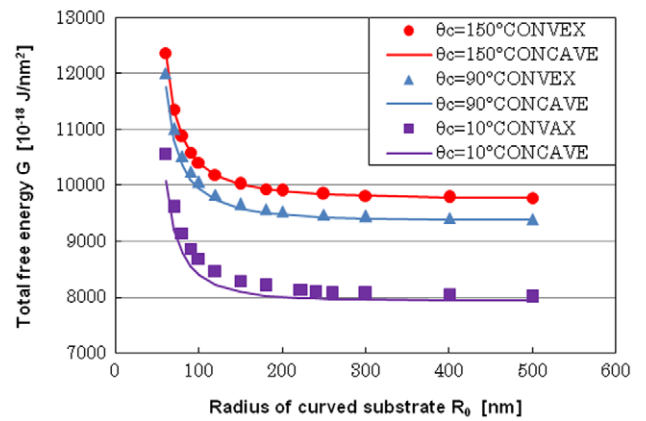

Figure 16. Effect of the curvature of the substrate on the total free energy G.

curved substrate. This difference of the free energy causes an attractive force on the metal film from a curved region to a flat region on a substrate. Since the curvature is small at the top of a mound, as seen in the experiment, a metal film is agglomerated on the top of the mound.

In addition, it is found that the total free energy decreases with decreasing contact angle. This is reasonable because dots of low contact angle are stable on the substrate. In the case of $\theta_c = 150°$, the difference of G between the convex substrate and the concave substrate is negligible. However, in the case of $\theta_c = 10°$, the difference of the free energies between the convex substrate and the concave substrate becomes apparent. G on the concave substrate is smaller than that of the convex substrate. A dot will be formed on a concave region when the contact angle becomes very small. However, in the present experiment, the contact angle of the gold and the quartz substrate is about 150° [42]. As a result, Au dots tend to be formed on the top of the convex part of the substrate.

Therefore it is concluded that the effect of curvature on the total free energy is one of the most influential mechanisms of dot aggregation on the top of the mound.

5. Conclusion

A new fabrication method of multilayer ordered nanodot arrays by combining top-down and bottom-up approaches was presented. The feasibility of the proposed method and mechanism of nanodot formation were investigated. The results are summarized as below.

(1) The effective parameters influencing the second-layer dot formation, including Au layer thickness and SiO_2 layer thickness, were investigated. The regularity and uniformity of second-layer nanodots are affected by the Au layer thickness. In addition, the thickness of the spacer layer influences the morphology of the second-layer nanodots. Good regularity is obtained when the thickness of the SiO_2 layer is between 50 and 200 nm. It was shown that dots are formed on the top of the mounds when the thickness of the metal layer and the spacer layer is ideal. A 3D nanodot array of good alignment was successfully fabricated by controlling the thickness of the metal layer and the SiO_2 spacer layer.

(2) The mechanism of nanodot agglomeration on the spacer layer was studied based on a geometrical model. The effects of the thickness of the metal layer were explained by the average dot size attributed to the holes on the deposited metal layer. The effects of the thickness of the spacer layer were explained by the topography of the spacer layer surface. Dot diameters on the mound and in the trough were calculated based on a geometrical model.

(3) The tendency of dot agglomeration on the mound was studied based on total free energy of the metal on a substrate. The mathematical model revealed that the total free energy of the system reduces more on a flat substrate than on a curved substrate. This difference of the free energy causes an attractive force on a metal film from a curved region to a flat region on a substrate. Since the surface curvature is small at the top of a mound, as seen in the experiment, the metal film is agglomerated on the top of the mound. The effect of surface curvature on the total free energy is one of the most influential mechanisms of dot formation on the top of the mound.

Acknowledgments

References

[1] Nozik A J 2010 Nanoscience and nanostructures for photovoltaics and solar fuels *Nano Lett.* **10** 2735–41

[2] Catchpole K R 2006 Nanostructures in photovoltaics *Phil. Trans. R. Soc.* A **364** 3493–503

[3] Ross C A 2001 Patterned magnetic recording media *Annu. Rev. Mater. Res.* **31** 203–35

[4] Lodder J C 2004 Methods for preparing patterned media for high-density recording *J. Magn. Magn. Mater.* **272–276** 1692–7

[5] Murry W A and Barnes W L 2007 Plasmonic materials *Adv. Mater.* **19** 3771–82

[6] Hutter E and Fendler J H 2004 Exploitation of localized surface plasmon resonance *Adv. Mater.* **16** 19

[7] Kneipp K, Kneipp H, Itzkan I, Dasari R R and Feld M S 2002 Surface-enhanced Raman scattering and biophysics *J. Phys.: Condens. Matter* **14** R597–624

[8] Hossain M K, Huang G G, Kaneko T and Ozaki Y 2009 Characteristics of surface-enhanced Raman scattering and surface-enhanced fluorescence using a single and a double layer gold nanostructure *Phys. Chem. Chem. Phys.* **11** 7484–90

[9] Li X, Zhang Y, Shen Z X and Fan H J 2012 Highly ordered arrays of particle-in-bowl plasmonic nanostructures for surface-enhanced Raman scattering *Small* **8** 2548–54

[10] Lakowicz J R *et al* 2004 Advances in surface-enhanced fluorescence *J. Fluoresc.* **14** 425–41

[11] Fort E and Gresillon S 2008 Surface enhanced fluorescence *J. Phys. D: Appl. Phys.* **41** 013001

[12] Pillai S, Catchpole K R, Trupke T and Green M A 2007 Surface plasmon enhanced silicon solar cells *J. Appl. Phys.* **101** 093105

[13] Catchpole K R and Polman A 2008 Plasmonic solar cells *Opt. Express* **16** 21793–800

[14] Gu X, Qiu T, Zhang W and Chu P K 2011 Light-emitting diodes enhanced by localized surface plasmon resonance *Nanoscale Res. Lett.* **6** 199

[15] Yeh D-M, Huang C-F, Chen C-Y, Lu Y-C and Yang C C 2008 Localized surface plasmon-induced emission enhancement of a green light-emitting diode *Nanotechnology* **19** 345201

[16] Anker J N, Hall W P, Lyandres O, Shah N C, Zhao J and Van Duyne R P 2008 Biosensing with plasmonic nanosensors *Nature Mater.* **7** 442–53

[17] Hong S, Kang T, Choi D, Choi Y and Lee L P 2012 Self-assembled three-dimensional nanocrown array *ACS Nano* **6** 5803–8

[18] Kim K H, Baek Y-K, Jeon H-J, Srinivasarao M and Jung H-T 2012 Cylindrical posts of Ag/SiO₂/Au multi-segment layer patterns for highly efficient surface enhanced Raman scattering *Nanotechnology* **23** 315302

[19] Zhang W, Ding F, Li W-D, Wang Y, Hu J and Chou S Y 2012 Giant and uniform fluorescence enhancement over large areas using plasmonic nanodots in 3D resonant cavity nanoantenna by nanoimprinting *Nanotechnology* **23** 225301

[20] Lin Y, Zou Y, Mo Y, Guo J and Lindquist R G 2010 *E*-beam patterned gold nanodot arrays on optical fiber tips for localized surface plasmon resonance biochemical sensing *Sensors* **10** 9397–406

[21] Han J, Kim T-G, Min B-K and Lee S J 2010 The fabrication of metal silicide nanodot arrays using localized ion implantation *Nanotechnology* **21** 485303

[22] Grossklausa K A and Millunchick J M 2011 Mechanisms of nanodot formation under focused ion beam irradiation in compound semiconductors *J. Appl. Phys.* **109** 014319

[23] Chou S Y, Krauss P R and Renstrom P J 1995 Imprint of sub-25 nm vias and trenches in polymers *Appl. Phys. Lett.* **67** 3114–6

[24] Chou S Y, Krauss P R and Renstrom P J 1996 Nanoimprint lithography *J. Vac. Sci. Technol.* B **14** 4129–33

[25] Park S K, Noh J S, Chin W B and Sung D D 2007 Fabrication of metal nanodot arrays using a porous alumina membrane as a template *Curr. Appl. Phys.* **7** 180–5

[26] Muller C M, Mornaghini F C F and Spolenak R 2008 Ordered arrays of faceted gold nanoparticles obtained by dewetting and nanosphere lithography *Nanotechnology* **19** 485306

[27] Lin C H, Jiang L, Chai Y H, Xiao H, Chen S J and Tsai H L 2010 A method to fabricate 2D nanoparticle arrays *Appl. Phys.* A **98** 855–60

[28] Zhong Z, Halilovic A, Fromherz T, Schaffler F and Bauer G 2003 Two-dimensional periodic positioning of self-assembled Ge islands on prepatterned Si (001) substrates *Appl. Phys. Lett.* **82** 4779–81

[29] Zhong Z and Bauer G 2004 Site-controlled and size-homogeneous Ge islands on prepatterned Si (001) substrates *Appl. Phys. Lett.* **84** 1922–4

[30] Giermann A L and Thompson C V 2005 Solid-state dewetting for ordered arrays of crystallographically oriented metal particles *Appl. Phys. Lett.* **86** 121903

[31] Giermann A L and Thompson C V 2011 Requirements for graphoepitaxial alignment through solid-state dewetting of Au films *J. Appl. Phys.* **109** 083520

[32] Osawa H, Yamanaka A, Kurnia W and Yoshino M 2011 Fabrication of ordered gold nano-dot array by using nano plastic forming and self-assembly *Trans. JSME* C **77** 1143–53

[33] Yoshino M, Osawa H and Yamanaka A 2011 Rapid fabrication of an ordered nano-dot array by the combination of nano-plastic forming and annealing methods *J. Micromech. Microeng.* **21** 125017

[34] Maenosono S, Okubo T and Yamaguchi Y 2003 Overview of nanoparticle array formation by wet coating *J. Nanopart. Res.* **5** 5–15

[35] Matsubayashi A, Fukunaga K, Tsuji T, Ataka K and Ohsaki H 2011 Multilayered ordering of the metal nanoparticles in polymer thin films under photoirradiation *Langmuir* **27** 733–40

[36] Jiang C, Markutsya S and Tsukruk V V 2004 Collective and individual plasmon resonances in nanoparticles films obtained by spin-assisted layer-by-layer assembly *Langmuir* **20** 882–90

[37] Springholz G 2005 Three-dimensional stacking of self-assembled quantum dots in multilayer structures *C. R. Physique* **6** 89–103

[38] Wang D and Schaaf P 2011 Two-dimensional nanoparticle arrays formed by dewetting of thin gold films deposited on pre-patterned substrates *J. Mater. Sci., Mater. Electron.* **22** 1067–70

[39] Henley S J, Carey J D and Silva S R P 2005 Pulsed-laser-induced nanoscale island formation in thin metal-on-oxide films *Phys. Rev.* B **72** 195408

[40] Kojima Y and Kato T 2008 Nanoparticle formation in Au thin films by electron-beam-induced dewetting *Nanotechnology* **19** 255605

[41] Trice J, Thomas D, Favazza C, Sureshkumar R and Kalyanaraman R 2007 Pulsed-laser-induced dewetting in nanoscopic metal films: theory and experiments *Phys. Rev.* B **75** 235439

[42] Sangiorgi R, Muolo M L, Chatain D and Eustathopoulos N 1988 Wettability and work of adhesion of nonreactive liquid metals on silica *J. Am. Ceram. Soc.* **71** 742–8